Investigation of the effects of thermal annealing on the structural, morphological and optical properties of nanostructured Mn doped ZnO thin films

Fouaz Lekoui[1*], Rachid Amrani[2,3], Walid Filali[4] , Elyes Garoudja[4], Lyes Sebih[2], Imad Eddine Bakouk[2], Hocine Akkari[5], Salim Hassani[1], Nadia Saoula[1], Slimane Oussalah[6], Hind Albalawi[7], Nourah Alwadai[7] and Mohamed Henini[8]

[1]Division milieux ionisés & Laser, Centre de Développement des Technologies Avancées, Cité 20 Août 1956, Baba Hassen, Alger, Algérie
[2] Département des sciences de la matière, Université Alger1 Ben youcef Benkhedda, Alger, Algérie
[3] LPCMME, Département de physique, Université d'Oran ES-Sénia, Oran, Algérie
[4]Plateforme Technologique de Micro-fabrication, Centre de Développement des Technologies Avancées, Cité 20 Août 1956, Baba Hassen, Alger, Algérie
[5]Département de Génie Industriel, Faculté de Technologie, Université Batna 2 Chahid Mostefa Ben Boulaid, rue Chahid Boukhlouf. M. El Hadi, Batna 05001, Algérie
[6]Division Microélectronique & Nanotechnologies, Centre de Développement des Technologies Avancées, Cité 20 Août 1956, Baba Hassen, Alger, Algérie
[7]Physics Department, Faculty of Science, Princess Nourah Bint Abdulrahman University, Riyadh, Saudi Arabia
[8]School of Physics and Astronomy, University of Nottingham, Nottingham, NG7 2RD, UK
[*]flekoui@cdta.dz

Abstract

The control of the optical properties of ZnO nanostructured thin films by using different dopant elements paves the way for the development of potential materials for photonic and optoelectronic applications. In this work manganese (Mn) doped ZnO thin films were fabricated by rapid thermal evaporation method on a glass substrate having the same Mn content level of ~10% and annealed at different temperatures. XRD analysis showed that the annealed layers have hexagonal wurtzite structure, however, the unannealed layers showed only Zn peaks without any preferential direction. The elemental analysis of the films has been investigated by XPS, which revealed the presence of Mn and oxygen atoms for all layers. In addition, it was observed by FIB-SEM that the morphology of thin films changed with the annealing temperature. For an anneal at 500°C nanoneedles appeared. Raman spectroscopy showed E_1 (TO) mode in the sample annealed at 500°C which was attributed with the formation of nanoneedles structures. The optical transmission of the annealed films was in the range of 75 - 77% and the optical bandgap varied from 3.97 to 3.72 eV. These variations are related to the structural and morphological changes of the thin films with annealing temperature.

Keywords MZO layers; Rapid thermal evaporation; Annealing temperature; Structural and optical properties; Nanoneedles; PSO algorithm.

1. Introduction

Zinc oxide (ZnO) has become an important material in wide different fields, due to its unique properties [1-4]. It is an intrinsic n-type semiconductor with a wide direct band gap of 3.37 eV and a large excitonic binding energy of 60 meV [5]. In addition, doping of ZnO with metallic elements results in an enhancement of its properties depending on the application field, such as silver (Ag) and aluminum (Al) for transparent conductive oxide (TCO) [6-8], magnesium (Mg) for breath analysis devices [9], mixture with another oxide like TiO_2 for Organic Blended Solar Cells Layers [10] and manganese (Mn) for Diluted Magnetic Semiconductors (DMS) or antibacterial thin films [11, 12].

Several works have studied Mn-doped ZnO thin films with various deposition techniques, namely chemical and physical methods such as spin coating [13], sol-gel [14], radio frequency magnetron sputtering [15], thermal evaporation [16] and pulsed laser deposition [17]. These techniques play a crucial role on the structural, morphological, optical or electrical characteristics of the layers.

The Mn-doped ZnO (MZO) system has attracted many researchers due to the high solubility of Mn in ZnO host material. The radii of Zn^{2+} (0.74 Å) and Mn^{2+} (0.80 Å) are very similar, and therefore Mn^{2+} can easily substitute Zn^{2+} sites without altering the original nature of ZnO structure [18]. However, this substitution influences the structural parameters and creates stress in the lattice, which affects the morphological and optical properties of ZnO. The doping concentration of Mn has a significant influence on the optical properties of ZnO [19, 20]. Thermal annealing strongly influences the solubility of Mn^{2+} ions into ZnO host matrix due to the presence of oxygen vacancies and the formation of secondary phases, which affect the optical properties of the thin films.

This study will report on the effect of thermal annealing temperature on the structural, morphological and optical properties of ZnO-Mn thin films deposited by rapid thermal evaporation of a mixture of ZnO and Mn powders. The ZnO lattice parameters “a” and “c”, the crystallites size “D”, the amount of oxygen through the O1s peak and the phonons vibration modes were investigated using X-rays diffraction (XRD), X-ray photoelectron spectroscopy (XPS), and Raman analysis, respectively. The morphological evolution of the nanostructured films were investigated by focused ion beam scanning electron microscopy (FIB-SEM). The optical properties of the thin films were analyzed by using optical transmission spectra obtained by a UV-Vis-NIR spectrophotometer. The optical constants such as the refractive index and absorption coefficient can be extracted from the transmission spectrum using the envelope method [21]. However, this method is useful only when the interference fringes are observed. In the present work, a novel method based on the Particle Swarm Optimization (PSO) algorithm [22] is applied in order to extract the most important optical constants using transmission spectrum without interference fringes. These optical constants will be then investigated as function of annealing temperature.

2. Experimental procedures

MZO thin films were deposited on ordinary glass substrates (stairway) of 1 mm thickness and 25×75 mm^2 surface area using thermal evaporation method. The thermal evaporation unit is homemade system, developed at our establishment. The crucible is heated by Joule effect to an appropriate temperature. The ZnO and Mn powders with a mixture mass ratio of (90:10) % and 99% purity for each powder were purchased from SIGMA-ALDRICH. The substrates were first cleaned in ultrasonic bath with acetone that was followed by a further clean in ethanol for 5 minutes. The deposition process was carried out at a low pressure of ~10^{-6} mbar by heating a crucible until reaching the sublimation temperature of ZnO powder of ~1600°C (flash deposition of a few seconds). The samples were then annealed under atmospheric pressure at three different temperatures 300, 400 and 500°C for one hour.

The structural and morphological properties were investigated by XRD, Raman spectroscopy, FIB-SEM, using Philips X'PertMP diffractometer (Cu-Kα, λ=1.54 Å) EA 125 Omicron, Lab Ram H-Resolution from Horiba Jobin Yvon and Helios Nano Lab TM 650, respectively. In addition, the elementary XPS characterization involved the use of a dual Mg/Al anticathode X excitation source without a monochromator. The main Kα emission lines of Mg and Al are 1253.6 eV and 1486.6 eV, respectively. The analyzer is a 125 mm radius hemisphere (EA 125 Omicron) with electrostatic optics that offers different focusing and magnification conditions. The excitation energy was set as 50 or 20 eV depending on the desired resolutions and counting rates. The optical transmittance of the deposited layers was investigated by OPTIZEN 3220UV spectrophotometer in UV-Visible-NIR range (200–1000 nm). From the transmittance curves, the optical constants were extracted by using a heuristic method based on PSO algorithm. Details about this method are given in the next section.

3. Particle Swarm Optimisation

Particle Swarm Optimization is a well-known and efficient optimization algorithm developed by Eberhart and Kennedy [22, 23]. It is an evolutionary computational strategy mainly inspired from the social comportment of bird flocking [24]. In this algorithm, each bird is called 'particle' and it is considered as a single solution within the search space. The whole birds fly with a specific velocity that directs them to find the global best solution. PSO mechanism is started by generating a set of random solutions and then updating them at each generation (cycle) till reaching the best optimal solutions. Moreover, PSO has been widely applied to solve a wide variety of difficult optimization problems [25-27]. In PSO, the full population of particles is called swarm, while the *ith* particle at the *kth* cycle is defined by the subsequent parameters:

- A present position within a search space of D dimension $X_i^k = (x_1^k, x_2^k, \dots, x_s^k, \dots, x_D^k)$, where x_s^k is in the range $[l_s, u_s]$, l_s and u_s denotes respectively the lower and upper variation boundaries of the *sth* particle.
- A present velocity V_i^k defined by $(v_1^k, v_2^k, \dots, v_s^k, \dots, v_D^k)$ and bounded by maximum and minimum velocity vectors V_{min}^k and V_{max}^k, respectively.

At each cycle, all particles may adjust the velocity vector on the basis of their personal best solution achieved so far P_{best} and the entire swarm's global best solution G_{best}.

The update of particles position and velocity is achieved as follows [22, 23]:

$$V_i(k+1) = wV_i(k) + c_1 r_1 \big(P_i(k) - X_i(k)\big) + c_2 r_2 \big(G(k) - X_i(k)\big) \tag{1}$$

$$X_i(k+1) = X_i(k) + V_i(k+1) \tag{2}$$

where X_i and V_i are the ith particle's position and velocity, respectively. w is the inertia weight. k is the iteration number. c_1 and c_2 are the acceleration constants and are usually employed to set the manner in which a particle will move. r_1 and r_2 are two random numbers in the range [0,1]. P_i is the *ith* particle's personal best position. G is the swarm's global best position.

The subsequent points summarize the main steps of PSO algorithm:

1. Initialize the particles by random velocity and positions
2. Compute the fitness function for each particle
3. Find and update P_{best} and G_{best}
4. Compute and update particles' velocity and positions
5. Repeat steps 2 to 4 until the stopping condition is met (sufficiently lower value of fitness or maximum number of cycles is reached)

It is important to point out that PSO is always influenced by several control parameters, including the problem dimension, number of particles (swarm size), acceleration coefficients and number of iterations. In this work, PSO algorithm was used to investigate the optical properties of ZnO-Mn thin films.

4. Results and discussion

4.1. XRD analysis

Figure 1 shows XRD spectra of as-grown and annealed ZnO-Mn layers. The annealing process was carried out at different temperatures, namely 300, 400 and 500°C. For the as-grown samples no peaks associated with ZnO and Mn were observed. However, Zn peaks at different directions were detected (002), (100), (101), (102) and (004), (JCPDS number 00-004-0784). During the evaporation process, the ZnO powder changes from a solid to a vapor state and the ZnO molecule is decomposed into Zn + O according to the equation: $ZnO \rightarrow Zn + 1/2\ O_2$ [28]. A large part of the released oxygen was pumped out by the pumping unit and the small amount of oxygen trapped by zinc during its condensation is not sufficient to form a ZnO phase detectable easily by the diffractometer [29-31]. We notice the appearance of ZnO (103) and very low intensity peaks which correspond to ZnO (100) and (002). After annealing, the zinc oxidation begins to be visible at 300°C and it becomes stronger with the increase in temperature at 500°C. One can see the appearance of ZnO wurtzite phase peaks according to the directions (101), (002), (100), (JCPDS Card No. 36-1451) and other peaks according to the following crystallographic directions: (110), (103) and (112). There are no peaks associated to Mn and MnO phases. Also, it is noticed that (101), (002) and (100) peaks shifted to lower angles, from 31.737°, 34.379°, 36.215° for pure ZnO to 30.67°, 34.356°,36.14° for our MZO films. This indicates an increase of the lattice parameters [32, 14], which is probably due to the substitution of Zn^{2+} (ionic radius = 0.074 nm) with larger radius Mn^{2+} (ionic radius= 0.080 nm), leading to larger ‘a’ and ‘c’ lattice parameters [33, 34].

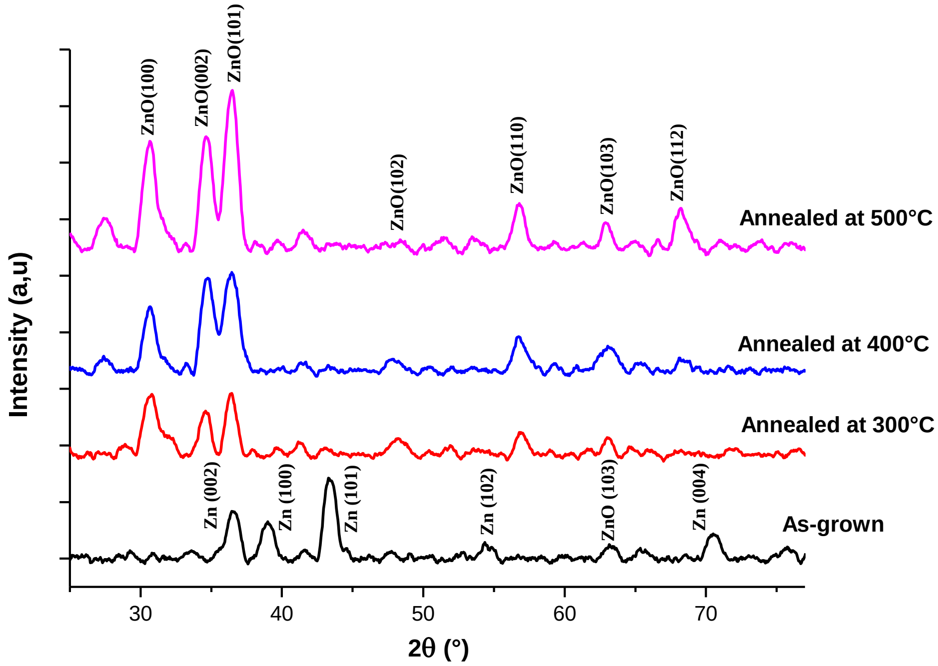

Fig. 1. XRD patterns of as-grown and annealed ZnO-Mn thin films.

For more insight on these structural modifications, the lattice parameters 'a' and 'c' are calculated based on Bragg relation [35]:

$$n\lambda = 2d_{hkl}.\ \sin\theta_{hkl} \qquad (3)$$

where h, k and l are Miller indices, θ_{hkl} is the diffraction angle, d_{hkl} and n are the inter-planar distance and diffraction order (n=0,1,2...), respectively.

In hexagonal wurtzite structure of ZnO, the inter-planar distance d_{hkl} is given by [36]:

$$\frac{1}{d_{hkl}^2} = \frac{4}{3}\left(\frac{h^2 + k^2 + hk}{a^2}\right) + \frac{l^2}{c^2} \qquad (4)$$

when n = 1, at the first order of approximation, the values of lattice parameters 'c' and 'a' are expressed by [37]:

$$c = \frac{\lambda}{sin\theta_{hkl}} \qquad (5)$$

$$a = \frac{\lambda}{\sin\theta_{hkl}\sqrt{3}} \qquad (6)$$

The distance between planes was found by using [38]:

$$d = \frac{\lambda}{2\sin\theta} \quad (7)$$

For further understanding of the structural changes, the crystallites size D, micro strain τ and dislocation density δ were determined by using the following formulas [39, 40]:

$$D = \frac{0.9\,\lambda}{FWHM.\cos\theta} \quad (8)$$

$$\tau = \frac{FWHM}{4\tan\theta} \quad (9)$$

$$\delta = \frac{1}{D^2} \quad (10)$$

where FWHM, θ and λ are full width at half maximum of XRD spectra, Bragg diffraction angle and wavelength of X-rays, respectively. To determine these parameters, (002) and (101) peaks for the annealed and as-grown MZO films, respectively, were selected. The strains toward c-axis ε_c and a-axis $\varepsilon_a$were calculated from the formula [41, 42]:

$$\varepsilon_c = \frac{(c-c_0)}{c_0} \times 100\% \quad (11)$$

$$\varepsilon_a = \frac{(a-a_0)}{a_0} \times 100\% \quad (12)$$

The bond length was calculated as follows [43]:

$$l = \sqrt{a^2/3 + (1/2 - u)^2 c^2} \quad (13)$$

where 'a_0' and 'c_0' are lattice parameters of pure ZnO. u is defined as positional parameter of the wurtzite structure that is given by [44]:

$$u = a^2/3c^2 + 0.25 \quad (14)$$

The bond angles α and β are given by [45]:

$$\alpha = \frac{\pi}{2} + cos^{-1}\left[\left(\sqrt{1 + 3\left(\frac{c}{a}\right)^2\left(\frac{1}{2} - u\right)^2}\right)^{-1}\right] \quad (15)$$

$$\beta = 2sin^{-1}\left[\left(\sqrt{\frac{4}{3} + 4\left(\frac{c}{a}\right)^2\left(\frac{1}{2} - u\right)^2}\right)^{-1}\right] \quad (16)$$

The values of lattice constants, inter-planar distance, micro strains, positional parameter, bond length and bond angles of MZO films obtained from XRD spectra are depicted in Table1. FWHM, crystallites size, lattice strain and dislocation density are listed in Table2.

Table 1.

Lattice constants 'a' and 'c', interplanar distance d, micro strains ε_a and ε_c, positional parameter u, bond length l and bond angles α, β of MZO films.

Annealing Temperature	c (nm)	a (nm)	Ratio c/a	d (nm)	ε_c	ε_a	l (nm)	u	α (°)	β (°)
300°C	0.5138	0.3366	1.5264	0.2568	-0.0128	0.036	0.201954	0.39306	105.7873	112.8905
400°C	0.5153	0.3377	1.5259	0.2575	-0.0099	0.039	0.203284	0.393159	105.7413	112.9064
500°C	0.5174	0.3393	1.5249	0.2588	-0.0059	0.044	0.203518	0.393348	105.7319	112.9374

Table 2.

FWHM, crystallites size D, lattice strain τ and dislocation density δ.

Annealing Temperature	FWHM (radian)	D (nm)	τ	$\delta(lines/nm^2)$ (10^{-3})
As-grown	0.015	9.92	0.009429	10.16
300°C	0.0098	14.86	0.007794	4.53
400°C	0.0097	14.91	0.007738	4.49
500°C	0.0068	21.50	0.005449	2.16

Figure 2 (a) and (b) shows the variation of FWHM, crystallites size and lattice parameters with annealing temperature. The value of 'c' is smaller than that of pure ZnO (c_0 = 0.5205 nm), which gives negatives values of micro strain along 'c' axis. This indicates that MZO films have tensile forces towards 'c' axis [46]. The lattice parameters 'a' and 'c' increase with increasing annealing temperatures. This may be due to an increase of the solubility of Mn atoms in the ZnO host lattice caused by the annealing process. Consequently, this generates more stress along 'c' and 'a' axis [47]. The FWHM and lattice strain of MZO films decrease as annealing temperature increases, providing evidence of an improvement of the crystalline quality of the layers [48]. The crystallites size of Mn-doped ZnO films changes from 9.92 nm (as-grown layers) to 21.5 nm (annealed at 500°C). This increase in crystallites size is due to an increase in the oxidation of the layers as a function of the annealing temperature. The smallest crystallites size is observed in the as-grown samples. This could be due to the low amount of incorporated oxygen, which makes a fine microstructure. However, at high annealing temperatures the crystallites become larger with higher probability of oxidation [49].

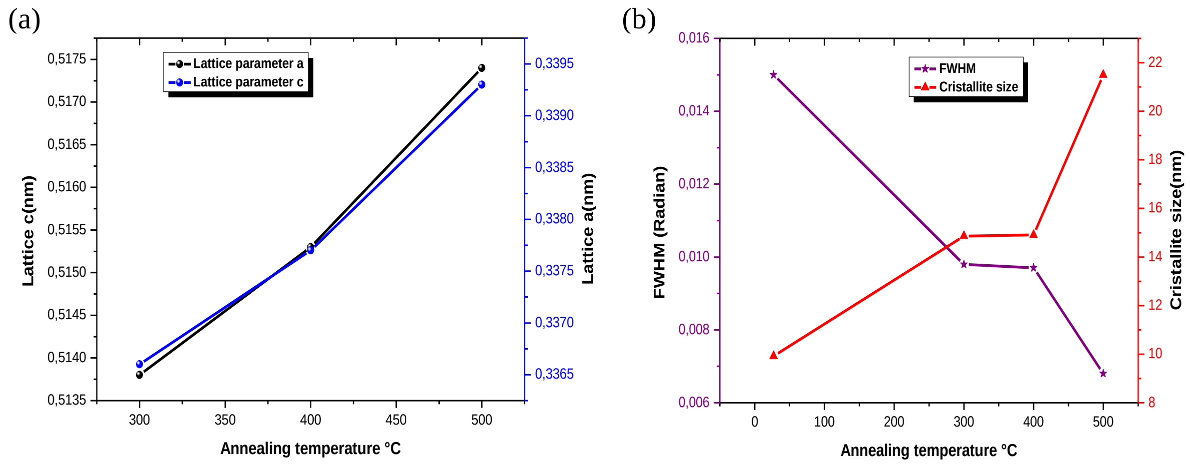

Fig. 2. Evolution of **(a)** lattice constants and **(b)** FWHM, crystallites size with annealing temperature.

As can be seen from Table 1, the values of bond length l, position parameter u and bond angles (α, β) increase as annealing temperature increases. The values of position parameter u are larger than the theoretical value (0.375) of pure ZnO. This can be accounted by the non-linearity of spontaneous polarization [50]. The increase in bond length l of MZO films with annealing temperature is probably due to the increase of Mn^{2+} solubility in the ZnO host lattice. It is also found that the bond angles α and β values are lower and higher than the ideal value of pure ZnO structure (109.47°), respectively. These differences are due to the differences in ionic radius and electronegativity between Mn and Zn atoms [51].

4.2. XPS analysis

XPS analysis was conducted to investigate the chemical composition and oxidation state of MZO thin films without and with annealing at 300, 400 and 500°C. The carbon 1s peak (290 eV) is used to calibrate the binding energies of XPS data. Figure 3 shows the XPS spectra of Zn2p and Mn2p of all layers, which confirm the presence of Zn and Mn elements in the films. The peaks of $Zn2p_{1/2}$ and $Zn2p_{3/2}$ are located at 1050 eV and 1027eV, respectively. The separation energy between both peaks (~23 eV) is detected. This indicates the existence of divalent oxidation state of Zn in as-grown and annealed films [52, 53]. However, there is a shift in the binding energy of $Zn2p_{1/2}$ and $Zn2p_{3/2}$, which can be attributed to the substitution of Zn^{2+} by Mn^{2+} ions and the formation of Zn-Mn bonding structure [54]. Figure 3 (b) shows that all samples, as-grown and annealed, have two peaks related to Mn, namely $Mn2p_{3/2}$ and $Mn2p_{1/2}$. The $Mn2p_{1/2}$ has a binding energy of 658.5 eV, which indicates the presence of Mn^{2+}

valence state in the substitution of Zn^{2+} ions. The difference in binding energy between $Mn2p_{3/2}$ and $Mn2p_{1/2}$ (~12.2 eV) confirms the oxidation state in the layers and the possibility of MnO_2 molecules existence [55, 56].

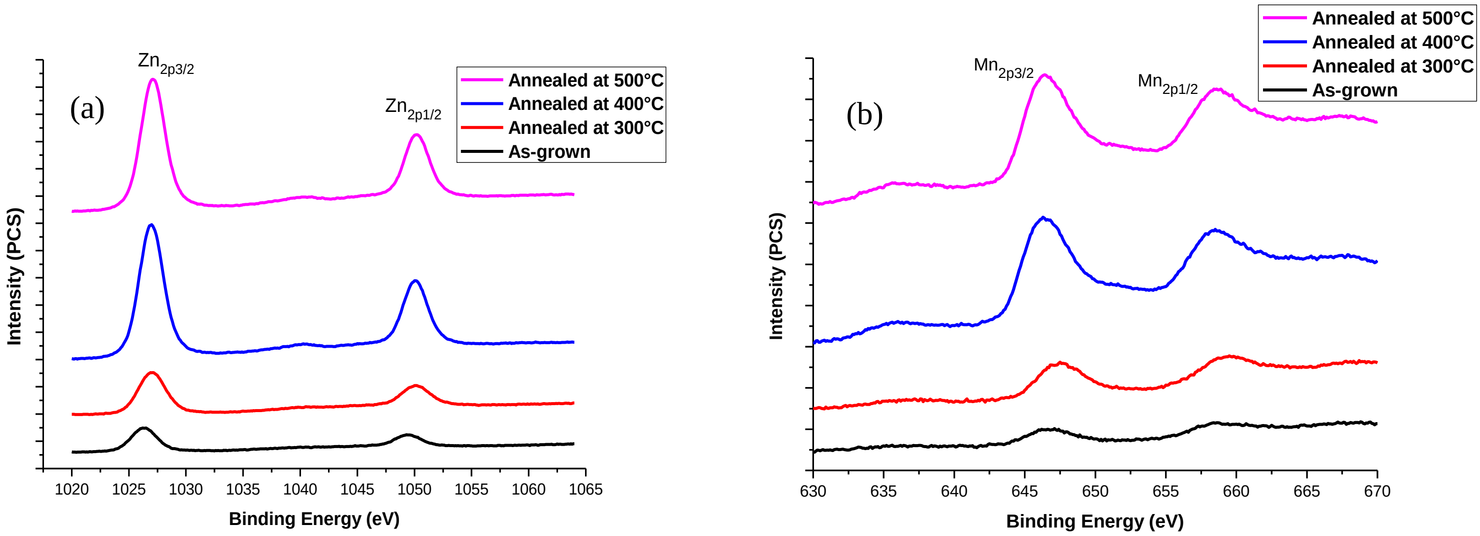

Fig. 3. XPS analysis of as-grown and annealed MZO films: (a) Zn2p and (b) Mn2p spectra of all samples.

Figure 4 illustrates the deconvolved peaks of the as-grown and annealed MZO layers. Firstly, we remark the presence of oxygen for the as-grown samples, which confirm our XRD analysis. Indeed, the small amount of oxygen in the film is insufficient to form ZnO phases detectable by XRD. The O1s peak of annealed layers shows a spectral contribution that was successfully disentangled by Gaussian fitting analysis, resulting in two components at 535.7 eV and 537 eV. The peak at lower binding energy was assigned to O^{2-} ions in Zn-O bonding of the wurtzite structure. Conversely, the peak at 537 eV was associated with O^{-} and O^{2-} ions in oxygen deficient regions in the ZnO matrix [57]. These defects play a crucial role in optical and luminescence properties of ZnO [58, 59]. With the increase of annealing temperature, the broad O1s peaks becomes more and more intense with a larger area, evidencing an increase of oxidation of the films and a decrease of the oxygen vacancies, as can be seen from the evolution of peak at 537 eV [60].

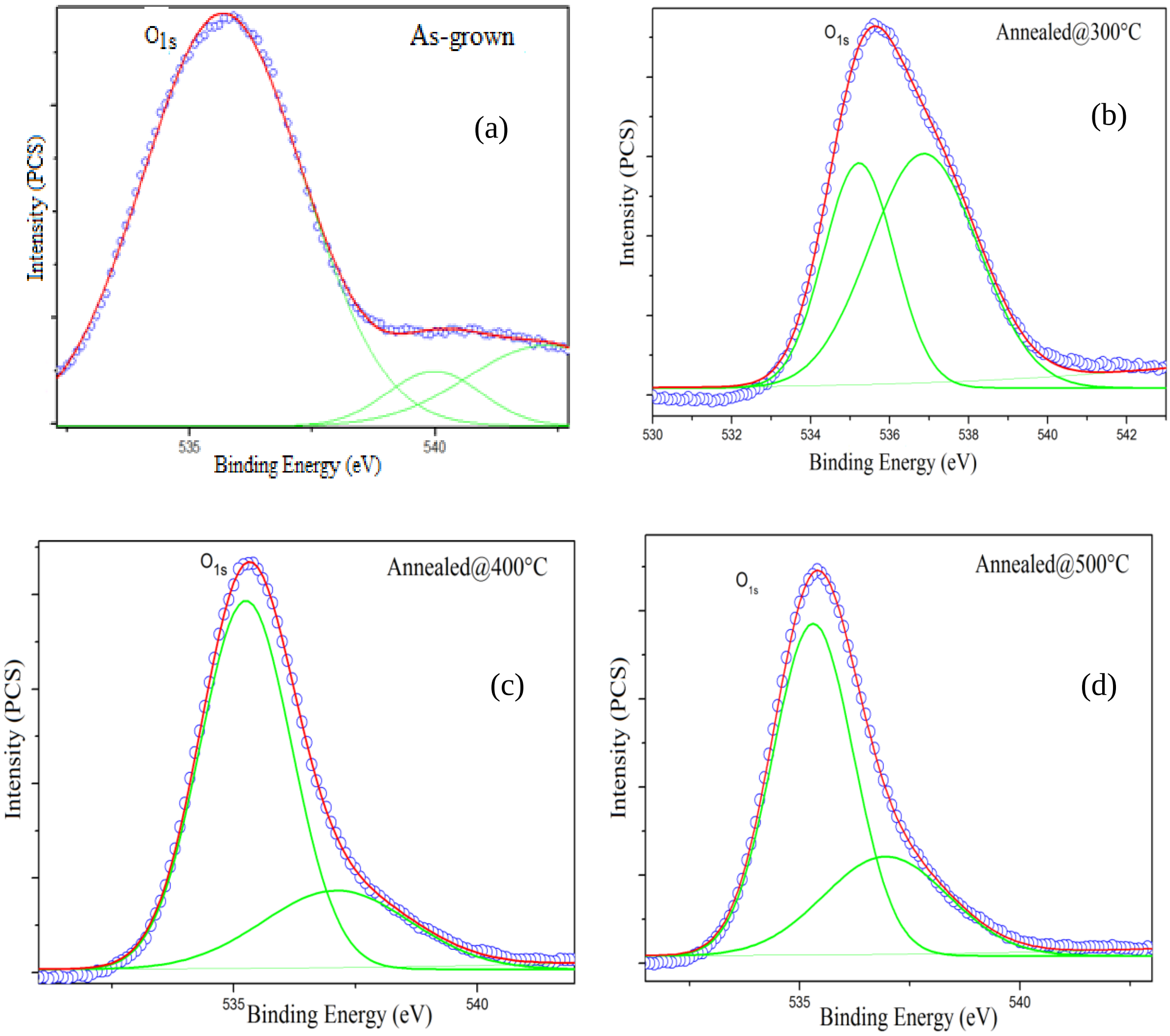

Fig. 4. XPS patterns of deconvolution O1s spectra for MZO samples: (a) as-grown and annealed at (b) 300°C, (c) 400°C, and (d) 500°C.

4.3. Surface Morphology

Figure 5 shows the morphological evolution with annealing temperature. The surface morphology was analyzed by FIB-SEM. In the literature, several approaches have been proposed to analyze the SEM images of thin films surfaces [61]. In our case, the authors have used the ImageJ software to analyze and calculate nanoparticles sizes. As can be seen from figure 5(a), the as-grown MZO films featured nanoparticles with irregular forms. The size of those nanoparticles changes from ~30 to ~70 nm. Figure 5(b) indicates that MZO films annealed at 300°C show a microsphere-like morphology, decorated with nanoparticles. Furthermore, with the increase of annealing temperature to 400°C, it is clearly that these microspheres become denser, and the nanoparticles disappeared. At 500°C, the surface morphology was completely changed, where the microspheres were transformed to nanoneedles, which are randomly distributed on the whole surface. These nanoneedles have a length around ~ 295 nm, and widths at the bottom and top of ~60.3 nm and ~ 25.8 nm, respectively. Similar nanostructures have been reported at this annealing temperature [62, 63].

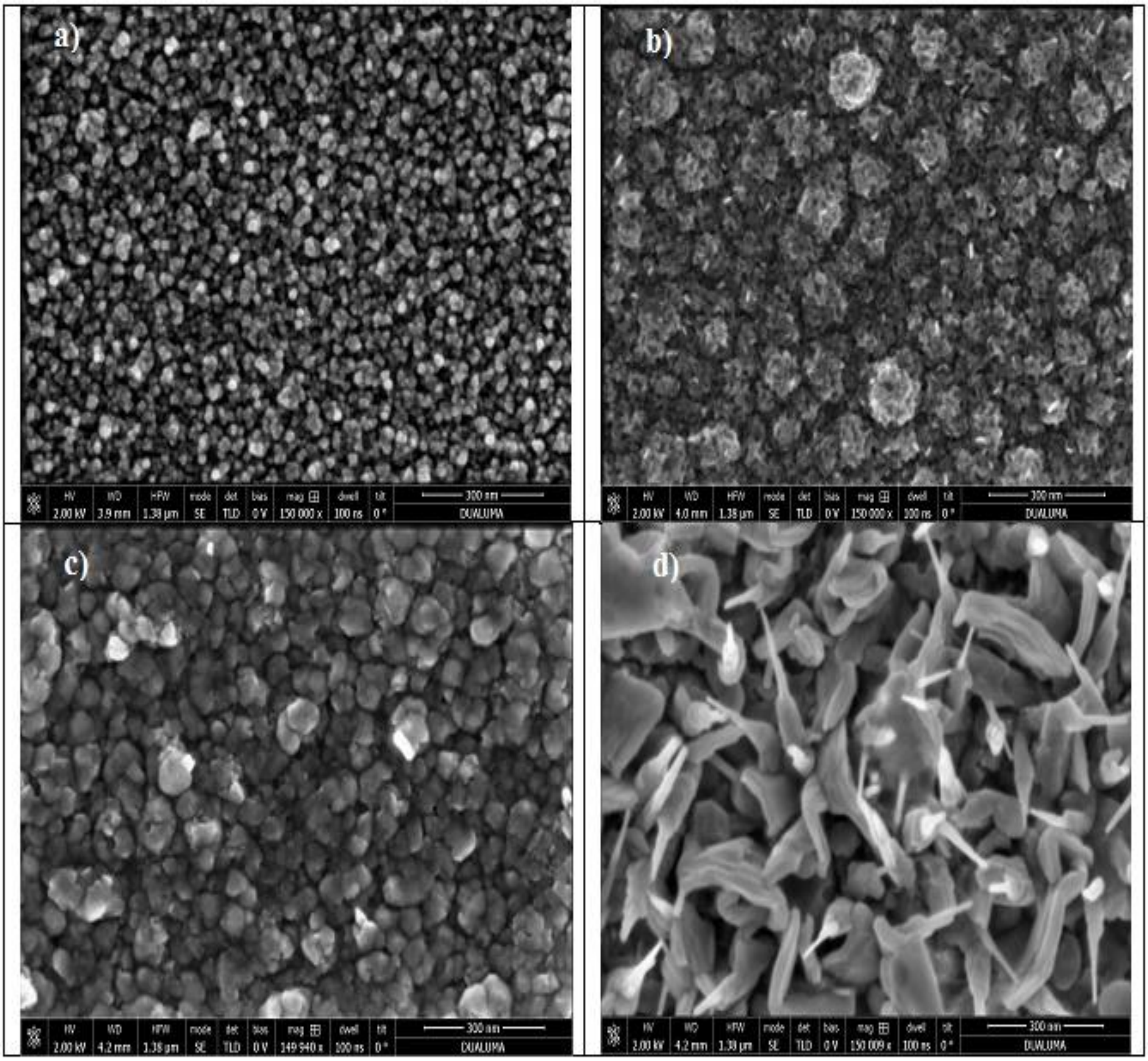

Fig. 5. FIB-SEM micrographs of a) as-grown MZO and annealed at b) 300°C, c) 400°C and d) 500°C.

4.4. Raman analysis

Figure 6 shows the Raman spectra of as-grown MZO samples and those annealed at 300, 400 and 500°C, which are deconvolved by Lorentzian distribution function. It is predicted that eight Raman modes of phonons symmetry exist for ZnO wurtzite structure [64], namely the singly and doubly degenerate modes of E_1, E_2, A_1 and B_1. In addition to these modes, there are acoustic and optical modes: $\Gamma_{aco} = A_1 + E_1$ and $\Gamma_{opt} = A_1 + (2 \times B_1) + E_1 + (2 \times E_2)$. B_1 is a known as a silent mode which cannot be observed in Raman spectra, while the others are actives modes [65]. A_1 (LO = longitudinal optical) mode was detected in all samples with a slight shift towards higher frequency. However, A_1 (TO = transverse optical) mode was detected with a shift towards the lower frequency. The A_1 phonon is polarized parallel to the c-axis of the wurtzite structure of ZnO, and the shift in frequency of this peak is due to the incorporation of Mn atoms in ZnO host lattice.

The E_2 (high) band is present in all samples, indicating the conservation of ZnO structure post-incorporation of Mn and thus confirming the XRD analysis results of the annealed samples. However, for the as-grown samples, the structure of ZnO was not observed by XRD but only by Raman. This could probably be due the resolution of the used diffractometer, and therefore a more detailed structural analysis is needed using High Resolution XRD (HR-XRD). Unlike XRD, Raman is sensitive to the degree of crystallinity in a sample. E_2 (high) peaks in all samples are smaller than that of pure ZnO. The frequency position of E_2 (high) phonons in our samples are shifted to higher frequency than that of pure ZnO (~ 437 cm^{-1}). This indicates the presence of tensile strain in the lattice and exactly in the perpendicular plane to the c-axis. This result is in good agreement with previous XRD studies [66, 67]. This interpretation could be supported by the observed peak at ~558 cm^{-1} which is present in all samples. According to Yadav et al [68], it is due to the activation of B_1 silent Raman modes (theoretical value is 520 cm^{-1}) resulting from the manganese substitution on oxygen sites, and/or Zn-O bond breaking caused by complex defects. These will induce a microscopic structural disorder in the Zn sub-lattice, causing the Raman modes activation around the Brillouin zone. The phonon modes are summarized in Table 3 and Table 4.

Table 3.

Peak analysis of Raman spectra of MZO layers

Peaks	E_2 (L) (cm^{-1})	A_1 (TO) (cm^{-1})	E_1 (TO) (cm^{-1})	E_2(high) (cm^{-1})	E_1 (LO) (cm^{-1})
Theoretical	101	380	407	437	583
As-grown samples	-	316	-	473	-
Samples annealed at 300°C	-	299	-	463	-
Samples annealed at 400°C	-	318	-	478	-
Samples annealed at 500°C	-	317	467	484	-

Table 4.

The rest of the identified Raman peaks of MZO layers

As-grown samples (cm^{-1})	Annealed at 300°C (cm^{-1})	Annealed at 400°C (cm^{-1})	Annealed at 500°C (cm^{-1})	Identification	references
555	558	558	561	Disorder caused by Mn^{2+} atoms (larger radius than that of Zn^{2+})	[69, 70]
809	781	797	799	Multi phonon modes of ZnO	[71]
884	886	888	887	Molecule with Mn	[71]

From figure 6, the observed peaks around (884, 886, 888 and 887 cm^{-1}) for all spectra could be attributed to Mn compounds ($ZnMnO_x$), such as $ZnMnO_3$ found by Toloman et al [70] at annealing temperature of 900°C. XPS analysis shows a probable presence of MnO_2 molecule. This compound was not observed by XRD analysis because its phase is certainly too weak to be detected. The increase in oxidation of the samples observed from XPS analysis is due to annealing performed in open air, which could possibly lead to an increase in the number of MnO_2 molecules. The large peaks at ~781 cm^{-1} especially for the annealed samples are attributed to processes involving a combination of LA + TO phonons of A_1 symmetry of ZnO [72].

Table 5 show the FWHM values of E_2 (high) bands for different samples. These values are higher compared to those reported for example by Wang et al [73] (FWHM=16 cm^{-1} for 2% Mn). This indicates that the samples have a low crystallinity. Our obtained results are in good agreement with those of Wang et al [72]. In fact, for a 5% Mn incorporation, the ZnO structure was destroyed and the peak becomes broader, which is reminiscent of that of an amorphous thin film. However, narrower FWHM and lower peak intensities at ~558 cm^{-1}, which are observed as the annealing temperature increases, indicate that the crystallinity of the samples is improved as confirmed by XRD analysis.

Table 5.

FWHM variation of E_2 (high) peak of MZO layers

Samples	As-grown samples	Samples annealed at 300°C	Samples annealed at 400°C	Samples annealed at 500°C
FWHM	129 cm^{-1}	126 cm^{-1}	92 cm^{-1}	39 cm^{-1}

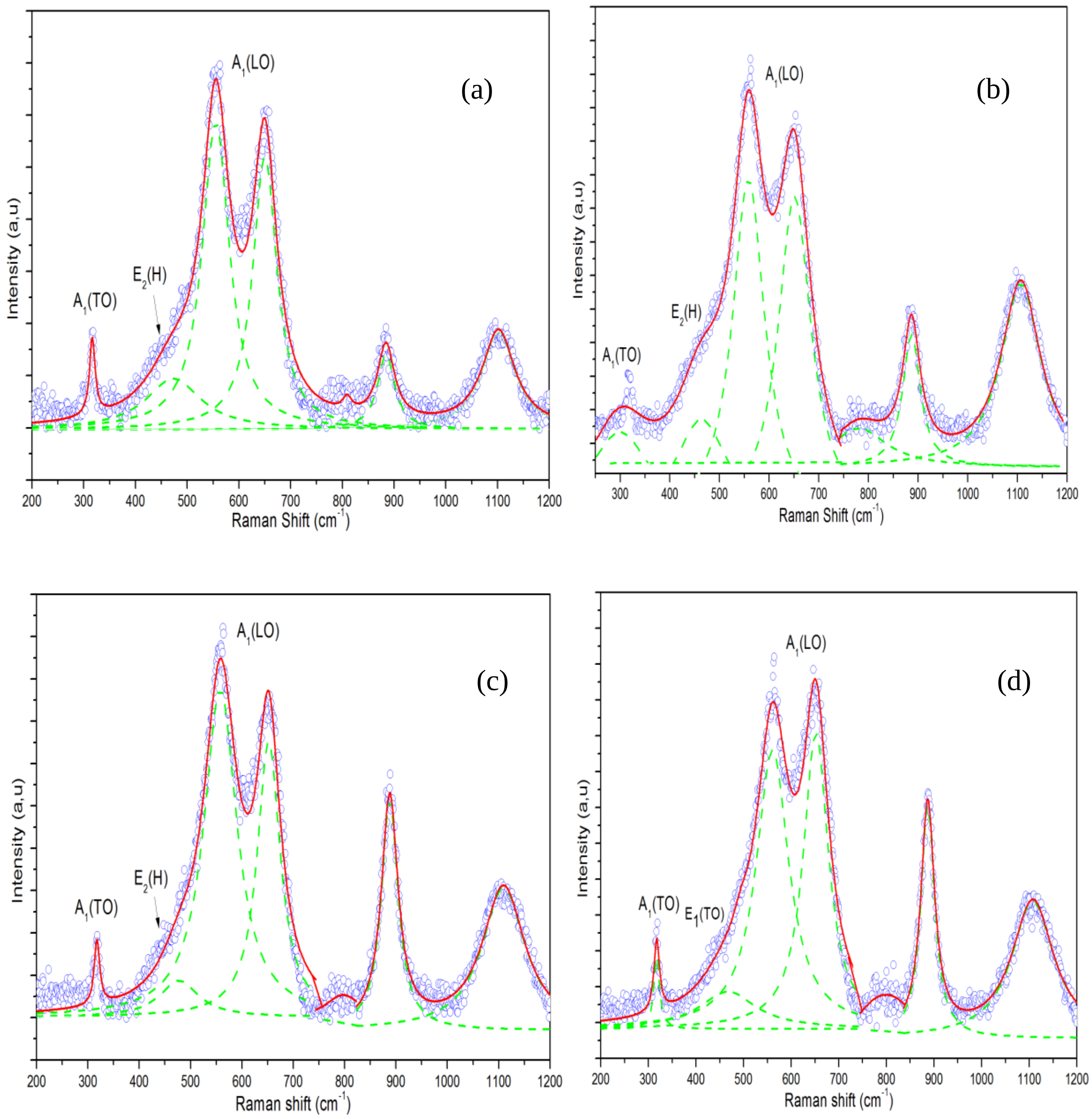

Fig. 6. Raman spectra with deconvolution of ZnO-Mn thin films (a) as-grown and annealed at (b) 300°C, (c) 400°C and (d) 500°C.

The peak at 467 cm^{-1} [E_1 (TO)] was observed only in the sample annealed at 500°C (Fig 6.d). It is worth pointing out that this sample displayed a different surface morphology as shown in the FIB-SEM micrograph in Figure 5(d), where the formation of needle-like nanostructures is clearly seen. In addition, the surface is decorated by nanoneedles without any preferential orientation and with a larger grain size than the other three samples (as-grown and annealed at 300^0C and 400^0C. Khan et al [73] observed the aforementioned peak in a sample with similar nanostructures and attribute it to the apparition of the E_1(TO) symmetry of ZnO.

4.5. Optical Properties

Figure 7 shows the optical transmission spectra of as-grown ZnO-Mn thin films and those annealed at 300, 400 and 500°C. These spectra were obtained by varying the wavelength in the range 200-1000 nm. The transmittance drops sharply in the UV region due to the fundamental absorption. It can be observed that the transmittance of as-grown films is less than 7% for all wavelengths, meaning that the films are practically opaque. However, the transmittance increases abruptly until reaching values between 72 and 77% with annealing. This increase in transmittance after annealing is due to the increase in the oxidation rate of ZnO, as discussed in the XRD and XPS analysis sections. In fact, an increase in the oxidation of the films with annealing temperature increasing has been reported before [74].

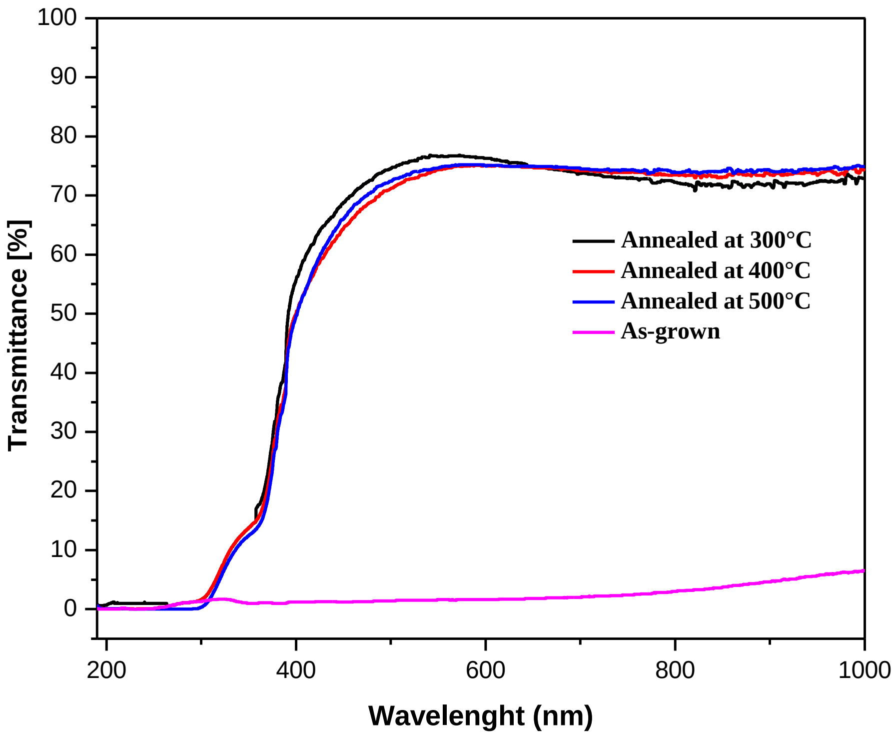

Fig. 7. Optical transmittance spectra of as-grown and annealed ZnO-Mn thin films.

In this work, the only use of transmittance spectra is sufficient to determine the ZnO-Mn thin film thickness and optical constants. Toward this end, the authors have treated the problem of thickness and optical constants determination in mathematical point of view. Indeed, it was considered as a minimization issue in which the function to be minimized (cost function) is defined by the Root-Mean-Square-Error (RMSE) between measured and estimated transmittance spectra. The obtained results accuracy is guaranteed by the sufficiently lowest value of RMSE that leads to a good fitting between both experimental and estimated spectra.

In this work, this function is called $h(\mu)$ and it is given as follows:

$$h(\mu) = \sqrt{\sum_{i=1}^{W} \left[T_{exp}(i) - T_{est}\,(i, \mu)\right]^2 / W} \qquad (17)$$

where T_{exp} and T_{est} denote experimental and estimated transmittance data, respectively. μ is the optimal parameters vector. Length of data included into the transmittance characteristic vector is denoted as W. The estimated transmittance spectrum was obtained by replacing the identified parameters (d, n) in the following theoretical model of transmittance [75]:

$$T = \frac{Ax}{B - Cx\cos\varphi + Dx^2} \qquad (18)$$

where

$$A = 16\, n_s(n^2 + k^2) \qquad (19)$$

$$B = [(n+1)^2 + k^2][(n+1)(n + {n_s}^2) + k^2] \qquad (20)$$

$$C = [(n^2 - 1 + k^2)(n^2 - {n_s}^2 + k^2) - 2k^2({n_s}^2 + 1)]2\,cos\,\varphi - k[2(n^2 - {n_s}^2 + k^2) + ({n_s}^2 + 1)(n^2 - 1 + k^2)]\,2\,sin\,\varphi \qquad (21)$$

$$D = [(n-1)^2 + k^2][(n-1)(n - {n_s}^2) + k^2] \qquad (22)$$

$$\varphi = \frac{4\pi nd}{\lambda} \qquad (23)$$

$$x = \exp(-\alpha\, d) \qquad (24)$$

In Equations (18-24), n_s and n are the substrate and thin film refractive indexes, respectively; d is the deposited film thickness; α is the absorption coefficients, λ is the wavelength and k is the extinction coefficient. To obtain the refractive index values, the Cauchy dispersion model have been used and it is given as [75]:

$$n(\lambda) = \alpha_1 + \frac{\beta_1}{\lambda^2} \qquad (25)$$

$$k(\lambda) = \alpha_2 + \frac{\beta_2}{\lambda^2} \quad (26)$$

where $\alpha_1, \beta_1, \alpha_2 and \beta_2$ are four fitting parameters.

The main idea is to determine first the optimal values of $\alpha_1, \beta_1, \alpha_2, \beta_2$ and d that minimize the cost function $h(\mu)$ based on the PSO algorithm. Then the refractive index will be computed by using Equation (25).

It important noting that first, the PSO algorithm will be applied in the region of medium and weak absorptions of the transmittance spectrum in order to determine the optical thickness (d) and Cauchy dispersion model parameters $(\alpha_1, \beta_1, \alpha_2, \beta_2)$. The values of n are then calculated from Equation (25) in the whole wavelength range. To prove the efficiency of this method, the PSO algorithm has been applied to the transmittance spectrum of ZnO-Mn thin films annealed at 300, 400 and 500°C. A detailed description will be illustrated for the sample annealed at 500°C. Moreover, as discussed in Section 3, the PSO algorithm has several control parameters to be fixed by the user. During this work, these values have been experimentally chosen by test/error strategy. This means that the efficiency of PSO algorithm has been tested for several values and only the best ones are selected. In this work, the authors have selected the following parameters:

1. Problem dimension = 5 (number of parameters to be determined)
2. Number of particles = 150 (swarm size)
3. Acceleration coefficients = 2
4. Inertia weight = 0.4
5. Number of iterations = 1500

The variation ranges of each parameter for the used PSO algorithm are given in Table 6.

Table 6.
Variation ranges of each parameter

Parameters	variation range
α_1	$[1 - 10]$
β_1	$[10^{+3} - 10^{+6}]$
α_2	$[10^{-5} - 10^{-2}]$
β_2	$[10^{+2} - 10^{+5}]$
d (nm)	$[60 - 800]$

The first stage consists of applying the PSO algorithm only in the weak and medium absorption zones. Figure 8 shows the measured and calculated (using PSO-based determined parameters) transmittance spectra in these zones. Table 7 summarizes the identification results and the reached RMSE value.

Table 7.
The determined parameters and the reached RMSE value

Parameters	${\alpha_1}^*$	${\beta_1}^*$	${\alpha_2}^*$	${\beta_2}^*$	d^*	$RMSE$
Value	2.05	$4.09\times10^{+04}$	2.31×10^{-3}	$2.15\times10^{+4}$	118.36	6.2×10^{-03}

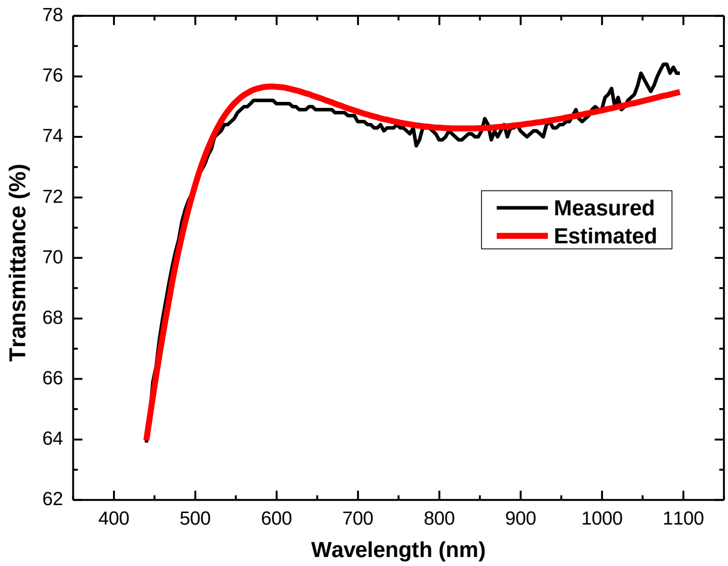

Fig. 8. Measured and estimated transmittance spectrum.

A good fitting between measured and estimated transmittance spectra has been observed in Figure 8. In addition, the results shown in Table 7 clearly demonstrate the high performance of the PSO algorithm to accurately determine the optical film thickness and Cauchy dispersion parameters. This accuracy is evidenced by the small RMSE value (6.2×10^{-03}).
Using parameters in Table 7, the refractive index can be re-written as:

$$n(\lambda) = 2.05 + \frac{4.09 \times 10^{+4}}{\lambda^2} \qquad (27)$$

This equation is used to extrapolate *n* for the entire wavelength range. The estimated values of *n* are depicted in Figure (9).

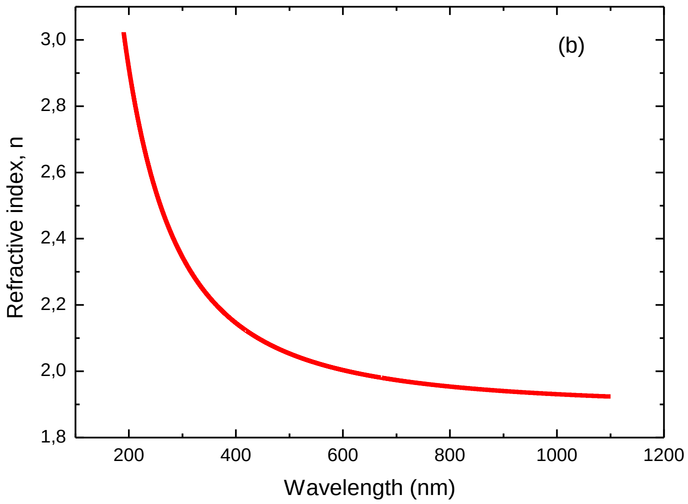

Fig. 9. The refractive index n dispersion for the whole wavelength range.

By making λ tends towards infinity in the Cauchy relation model expressed by equation (27), the static refractive index can be determined. The obtained values are 2.12, 2.04 and 2.055 for the samples annealed at 300, 400 and 500°C, respectively. It is worth mentioning that a thickness of ~118 nm was determined optically. The values of the refractive index at λ = 600 nm are found to be 2.148, 2.070 and 2.081 for the samples annealed at 300, 400 and 500°C, respectively.

The optical absorption coefficient α is determined in the area of high absorption using the relationship [76]:

$$\alpha = -\frac{1}{d}\ln\left(\frac{B}{A}T\right) \qquad (28)$$

The refractive index in this region is obtained by extrapolation of the index values obtained in the region of low absorption by Cauchy dispersion relationship.

Figure 10 presents the variation of α as a function of the energies of the incident photons. It is clearly seen that the values of α are greater than 10^4 cm^{-1}, confirming that the probability of direct electronic transitions is very high, as reported previously [77].

It emerges from Figure 10 that the absorption coefficient gradually increases with increasing photon energy hν ≤ 3.3 eV, and then increases sharply for hν =3.3-3.9 eV. This sharp increase, which is the result of the transition of electrons from the valence band to the conduction band, helps in determining the absorption threshold more accurately, and consequently the energy band gap value.

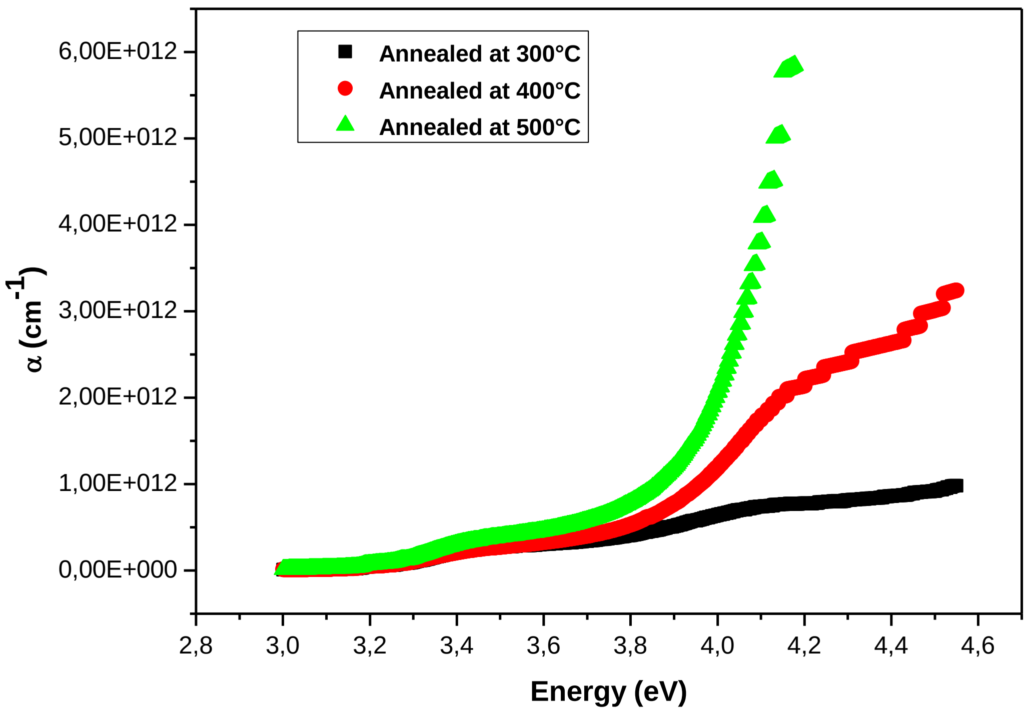

Fig. 10. Variation of the absorption coefficient α as a function of the incident photons energy.

Using the absorption coefficient α, the energy band gap (E_g) of the MZO thin films can be determined. ZnO-Mn films have a direct gap, and therefore the following formula can be used to calculate E_g of MZO thin films [78]:

$$\alpha h\upsilon = A' \sqrt{h\upsilon - Eg} \qquad (29)$$

where A' is a constant, and hυ is the incident photon energy. Eg is generally obtained by extrapolation of the linear part of $(\alpha h\upsilon)^2$ versus hυ plot to αhυ = 0, as shown in Figure 11 for the samples annealed at 400°C. Figure 12 shows the variation of E_g values for different annealed samples. E_g gradually decreases from 3.97 eV to 3.72 eV with temperature increase from 300 to 500°C. Compared with E_g value of pure ZnO ($E_g \sim$ 3.37 eV), MZO films have higher E_g values. This can be attributed to the structural modification and deformation of ZnO via Mn incorporation into the host lattice.

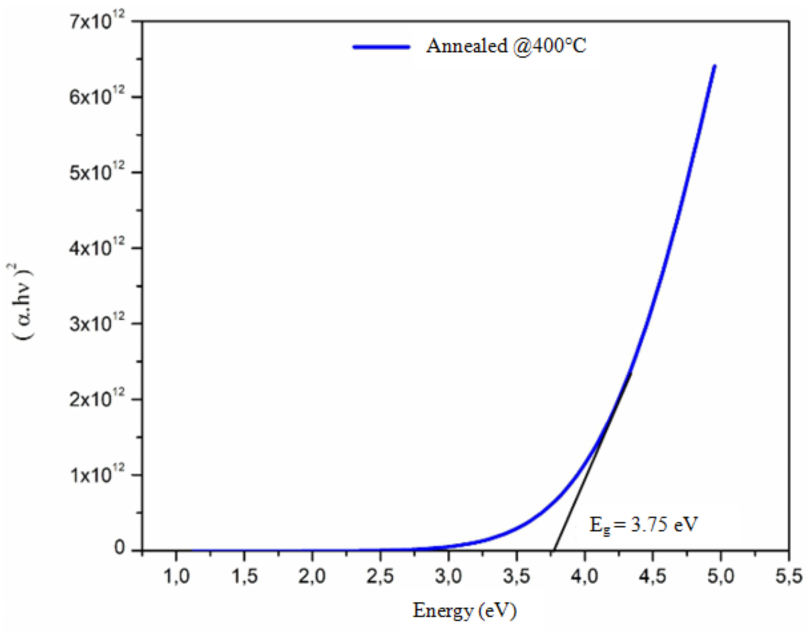

Fig. 11. Example of extrapolation of linear part of $(\alpha h\upsilon)^2$ versus $h\upsilon$ plot to $\alpha h\upsilon = 0$ to determine E_g of the samples annealed at 400°C.

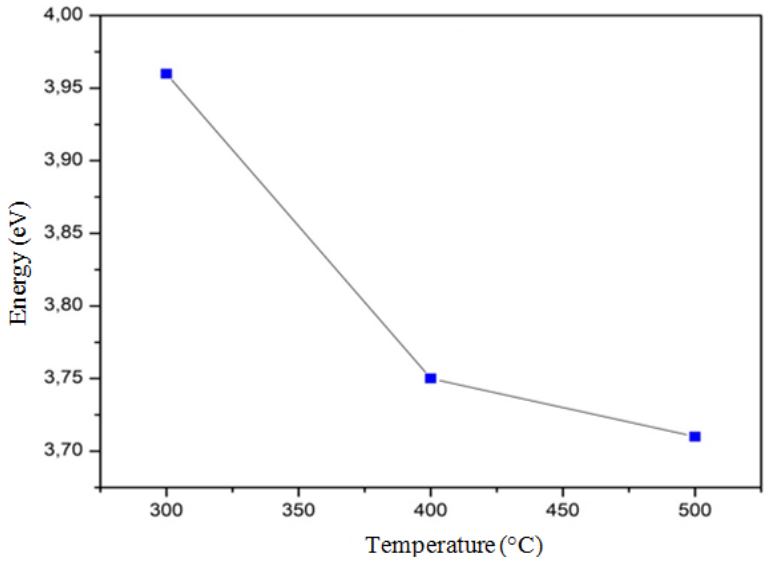

Fig. 12. Variation of E_g as function of the annealing temperature.

5. Conclusion

In this work, a systematic investigation of structural, morphological and optical properties as function of annealing temperature of MZO thin films was carried out. The samples were prepared by rapid thermal evaporation of ZnO and Mn powders mixture. XRD analysis revealed that MZO layers after annealing crystallize in hexagonal wurtzite phase with an increase in lattice parameters and crystallites size. XPS analysis showed the presence of Mn atoms, which caused a degradation of the structure and the quality of the thin films. The

Mn atoms that are not substituted on Zn^{2+} sites cause the formation of impurity phases as Zn-Mn or MnO_2. FIB-SEM images showed that the morphology of the MZO thin films was affected by the annealing process. For a 500°C thermal anneal, nanoneedles were formed without any preferential orientation. Raman measurements have also shown an additional mode E_1 (TO) at 467 cm^{-1} associated with the apparition of nanoneedles. The as-grown samples were found to be opaque with a very low transmittance. However, the average optical transmittance for the annealed MZO layers after annealing was enhanced with values above 77%. The optical constants n, α and the thickness d were successfully identified and determined from the transmittance spectra using the PSO algorithm. The energy band gap E_g was computed for different annealing temperatures. The obtained results showed that E_g decreases from 3.97 to 3.72 eV with increasing annealing temperature from 300 to 500°C. Finally, this study allows a better understanding of MZO material properties, in order to well use it in different fields of application, particularly in solar cells and antibacterial activities.

Acknowledgments

We are grateful for Prof Francisco de Paula Martín Jiménez, from university of Malaga (Spain) for his assistance during FIB-SEM analysis. Grateful are also addressed to Rémi Lazzari Alain from Institut de nanosciences de Paris (INSP) (France) and Naitbouda Abdelyamine from CDTA (Algérie) for their helpful in XPS and Raman analysis.

References

[1] Y.S. Kim, W.P. Tai and S.J. Shu. Effect of preheating temperature on structural and optical properties of ZnO thin films by sol–gel process. Thin Solid Films. 491 (2005) 153-160. https://doi:10.1016/j.tsf.2005.06.013

[2] H. Cao, J.Y. Xu, E.W. Seelig and R.P.H Chang. Microlaser made of disordered media. Appl. Phys. Lett. 76 (2000) 2997. https://doi.org/10.1063/1.126557

[3] Deng Rui, Zou Youming and Tang Honggao. Correlation between electrical, optical properties and Ag^{+2} centers of ZnO:Ag thin films. Physica B. 403 (2008) 2004–2007. https://doi.org/10.1016/j.physb.2007.11.007

[4] Ş. Ţălu, Micro and nanoscale characterization of three dimensional surfaces. Basics and applications. Napoca Star Publishing House, Cluj-Napoca, Romania, 2015.

[5] Yao-Ming Hao, Shi-Yun Lou, Shao-Min Zhou, Rui-Jian Yuan, Gong-Yu Zhu and Ning Li. Structural, Optical and magnetic studies of manganese doped zinc oxide hierarchical microspheres by self assembly of nanoparticles. Nano. Resea. Lett. 7 (2012) 100. https://doi.org/10.1186/1556-276X-7-100

[6] A. Arunachalama, S. Dhanapandianb and M. Rajasekaran. Morphology controllable flower like nanostructures of Ag doped ZnO thin films and its application as photovoltaic material. Journal of Analytical and Applied Pyrolysis. 123 (2017) 107-117. https://doi.org/10.1016/j.jaap.2016.12.019

[7] Afrina Sharmin, Samia Tabassum, Bashar MS and Zahid Hasan Mahmood. Depositions and characterization of sol–gel processed Al-doped ZnO (AZO) as transparent conducting oxide (TCO) for solar cell application. Journal of Theoretical and Applied Physics. 13 (2019) 123–132. https://doi.org/10.1007/s40094-019-0329-0

[8] Ştefan Ţălu, Miroslaw Bramowicz, Slawomir Kulesza, Shahram Solaymani, Atefeh Ghaderi, Laya Dejam, Seyed Mohammad Elahi and Arash Boochani. Microstructure and Micromorphology of ZnO Thin Films: Case Study on Al Doping and Annealing Effects. Superlattices and Microstructures. 93 (2016) 109-121. http://DOI:10.1016/j.spmi.2016.03.003

[9] S. Goudarzi and K. Khojier. Role of substrate temperature on the ammonia gas sensing performance of Mg-doped ZnO thin films deposited by spray pyrolysis technique: application in breath analysis devices. Applied Physics A. 124 (2018) 601. https://doi.org/10.1007/s00339-018-2020-8.

[10] Stefan Talu, Sebastian Stach, Muhammad Ikram, Dinesh Pathak, Tomas Wagner and Jean-Michel Nunzi. Surface Roughness Characterization of ZnO: TiO_2-Organic Blended Solar Cells Layers by Atomic Force Microscopy and Fractal Analysis. International Journal of Nanoscience. 13 (2014) 1450020. http://DOI:10.1142/S0219581X14500203

[11] Shenghong Yang and Yueli Zhang. Structural, optical and magnetic properties of Mn doped ZnO thin films prepared by Sol-Gel method. Journal of Magnetism and Magnetic Materials. 334 (2013) 52-58. http://dx.doi.org/10.1016/j.jmmm.2013.01.026

[12] K. Rekha, M. Nirmala, Manjula, G. Nair, A. Anukaliani. Structural, optical, photocatalytic and antibacterial activity of zinc oxide and manganese doped zinc oxide nanoparticles. Physica B. 405 (2010) 3180–3185. http://doi:10.1016/j.physb.2010.04.042

[13] Y. Caglar, S. Ilican, M. Caglar and F. Yakuphanoglu. Influence of Mn incorporation on the structural and optical properties of sol gel derived ZnO film. J. Sol. Gel. Sci and technology. 53 (2010) 372-377. http://DOI:10.1007/s10971-009-2105-0

[14] XuLi, Xinghua Zhu, Kangxin Jin and Dingyu yang. Study on structural and optical properties of Mn doped ZnO thin films by sol-gel method. Optical Materials. 100 (2020) 109657. https://doi.org/10.1016/j.optmat.2020.109657

[15] K.K. Nagaraja, S. Pramodini, P. Poornesh, Ashok Rao, H.S. Nagaraja. Influence of annealing on the linear and nonlinear optical properties of Mn doped ZnO thin films examined by z-scan technique in CW regime. Optical Materials. 58 (2016) 373-381. https://doi.org/10.1016/j.optmat.2016.06.008

[16] G.G. Rusu, P. Gorley, C. Baban, A.P. Rambu, M. Rusu. Preparation and characterization of Mn doped ZnO thin films. Journal of Microelectronics and advanced materials. 12 (2010) 895-899.

[17] J. Zhang, X.Z. Li, J. Shi, Y.F. Lu and D.J. Sellmyer. Structure and magnetic properties of Mn-doped ZnO thin films. J. Phys : Condensed matter. 19 (2007) 036210. http://DOI:10.1088/0953-8984/19/3/036210

[18] Dhruvashi, M. Tanemura and P.K. Shishodia. Ferromagnetism In Sol-Gel Derived ZnO:Mn Nanocrystalline Thin Films. Advanced Materials Letters. 7 (2016) 116-122. http://DOI:10.5185/amlett.2016.5966

[19] S.V. Bhat and F.L. Deepak. Tuning the bandgap of ZnO by substitution with Mn^{2+}, Co^{2+} and Ni^{2+}. J. Solid State Commun. 135 (2005) 345. http://doi:10.1016/j.ssc.2005.05.051

[20] R. Viswanatha, S. Sapra, S.S. Gupta, B. Satpati, P.V. Satyam, B.N. Dev and D.D. Sarma. Synthesis and Characterization of Mn Doped ZnO Nanocrystals. J. Phys. Chem. B. 108 (2004) 6303. http://DOI:10.1021/jp049960o

[21] R. Swanepoel. Determination of the thickness and optical constants of amorphous silicon. J.Phys. E: Sci. Instrum. 16 (1983) 1214-1222. https://doi.org/10.1088/0022-3735/16/12/023

[22] R. Eberhart and J. Kennedy. Particle swarm optimization In Proceedings of the IEEE international conference on neural networks. 4 (1995) 1942-1948.

[23] R. Eberhart and J. Kennedy. A new optimizer using particle swarm theory. In MHS'95. Proceedings of the Sixth International Symposium on Micro Machine and Human Science. (1995) 39-43.

[24] X.B. Meng, X.Z. Gao, L. Lu, Y. Liu and H. Zhang. A new bio-inspired optimisation algorithm: Bird Swarm Algorithm. Journal of Experimental & Theoretical Artificial Intelligence. 28 (2016) 673-687.

[25] Y. Wei and L. Qiqiang. Survey on Particle Swarm Optimization Algorithm. J. Engineering Science. 5 (2004) 87-94.

[26] M.R. AlRashidi and M.E. El-Hawary. A survey of particle swarm optimization applications in electric power systems IEEE transactions on evolutionary computation. 13 (2008) 913-918. http://DOI:10.1109/TEVC.2006.880326

[27] S. Sarkar, A. Roy and B.S. Purkayastha. Application of particle swarm optimization in data clustering: a survey. International Journal of Computer Applications. 65 (2013) 38-46. http://doi:10.5120/11276-6010

[28] B.V. L'vov, V.L. Ugolkov and F.F. Grekov. Kinetics and mechanism of free-surface vaporization of zinc, cadmium and mercury oxides analyzed thermogravimetrically by the third-law method. Thermochim. Acta. 411 (2004) 187–93. http://doi:10.1016/j.tca.2003.08.024

[29] F. Lekoui, M. Ouchabane, H. Akkari, S. Hassani and D. Dergham. Effect of annealing temperature on the properties of Ag doped ZnO thin films. Mater. Res. Express. 5 (2018) 106406. https://doi.org/10.1088/2053-1591/aadafa

[30] F. Lekoui, M. Ouchabane, S. Hassani, H. Akkari, D. Dergham, N. Saoula, L. Henni, and S. Abdelmoumen Structural, Optical, Electrical and Mechanical Properties of ZnO Co-doped Ag, Mg Thin Films: Annealing Temperature Effect ISMSD 2019, Proceedings of the 4th International Symposium on Materials and Sustainable Development. Springer Nature, Switzerland AG. (2020) 184-192. https://doi.org/10.1007/978-3-030-43268-3_16

[31] Fouaz Lekoui, Salim Hassani, Mohammed Ouchabane, Hocine Akkari, Driss Dergham, Walid Filali and Elyes Garoudja. Elaboration and Characterization of Mg-Doped ZnO Thin Film by Thermal Evaporation: Annealing Temperature Effect. Brazilian Journal of Physics. (2021) 1-9. https://doi.org/10.1007/s13538-021-00866-y

[32] M. Mazhdi, J. Saydi, M. Karimi, J. Seidi and F. Mazhdi. A study on optical, photoluminescence and thermoluminescence properties of ZnO and Mn doped ZnO nanocrystalline particles. Optik. 124 (2013) 4128-4133. http://dx.doi.org/10.1016/j.ijleo.2012.12.068

[33] Shenghong Yang and Yueli Zhang. Structural, optical and magnetic properties of Mn doped ZnO films prepared by sol-gel method. Journal of Magnetism and Magnetic Materials. 334 (2013) 52-58. http://dx.doi.org/10.1016/j.jmmm.2013.01.026

[34] J. Anghel, A. Thurber, D.A. Tenne, C.B. Hanna and A. Punnoose. Correlation between saturation magnetization, bandgap, and lattice volume of transition metal (M = Cr, Mn, Fe, Co, or Ni)

doped $Zn_{1-x}M_xOZn_{1-x}M_xO$ nanoparticles. Journal of Applied Physics. 107 (2010) 09E314. https://doi.org/10.1063/1.3360189

[35] M.E. Fragala and G. Malandrino. Characterization of ZnO and ZnO:Al films deposited by MOCVD on oriented and amorphous substrates. Microelectronics Journal. 40 (2009) 381-384. https://doi.org/10.1016/j.mejo.2008.09.003

[36] X. Wang, J. Sang and Z.L. Wang. Nanowire and nanobelt arrays of zinc oxide from synthesis to properties and to novel devices. Journal of Materials Chemistry. 17 (2007) 711- 720. https://doi.org/10.1039/B616963P

[37] M. Caglar, Y. Caglar and S. Ilican. The determination of the thickness and optical constants of the ZnO crystalline thin films by using envelope method. J Optoelectron Adv Mater. 8 (2006) 1410-3.

[38] M. Kashif, U. Hashim, M.E. Ali, S.M. Usman Ali, M. Rusop, Z.H. Ibupoto and al. Effect of different seed solutions on the morphology and electro-optical properties of ZnO Nanorods. J Nanomater. 1-6 (2012). http://doi:10.1155/2012/452407

[39] J. Li, D. Yang, X. Zhu, H. Sun, X. Gao, P. Wangyang and H. Tian. Structural and optical properties of nano-crystalline ZnO thin films synthesized by sol–gel method. J Sol-Gel. Sci. Technol. 82 (2017) 563–8. https://doi.org/10.1007/s10971-017-4335-x

[40] A. Goktas, A. Tumbul, Z. Aba and M. Durgun. Mg doping levels and annealing temperature induced structural, optical and electrical properties of highly c-axis oriented ZnO:Mg thin films and Al/ ZnO:Mg/p-Si/Al heterojunction diode. Thin Solid Films. 680 (2019) 20-30. http://doi.org/10.1016/j.tsf.2019.04.024

[41] L. Xu, X. Li, Y. Chen and F. Xu. Structural and optical properties of ZnO thin films prepared by sol-gel method with different thickness. Appl Surf Sci. 257 (2011) 4031–7. http://doi:10.1016/j.apsusc.2010.11.170

[42] O.F. Farhat, M.M. Halim, M.J. Abdullah, M.K.M. Ali and N.K. Allam. Morphological and structural characterization of single-crystal ZnO nanorod arrays on flexible and non-flexible substrates Beilstein. J Nanotechnol. 6 (2015) 720–725. http://doi:10.3762/bjnano.6.73

[43] G. Srinivasan, R.T. Rajendra Kumar and J. Kumar. Li doped and undoped ZnO nanocrystalline thin films: a comparative study of structural and optical properties. J Sol-Gel Sci Technol. 43 (2007) 171–7. http://doi:10.1007/s10971-007-1574-2

[44] R. Mariappan, V. Ponnuswamy, A. Chandra Bose, A. Chithambararaj, R. Suresh and M. Ragavendar. Structural, optical and electrical characterization of nebulizer-sprayed ZnO nano-rods. Superlattices Microstruct. 65 (2014) 184–94. http://doi:10.1016/j.spmi.2013.10.005

[45] H. Morkoç. Handbook of nitride semiconductors and devices.Volume 1, Materials, properties, physics and growth. Wiley-VCH (2008).

[46] D. Fang, C. Li, N. Wang, P. Li and P. Yao. Structural and optical properties of Mg-doped ZnO thin films prepared by a modified Pechini method. Cryst Res Technol. 48 (2013) 265-272. http://doi:10.1002/crat.201200437

[47] D. Igor, G. George, A. Denis, P. Matej, J. Zvonko and N. Markus. Diluted magnetic semiconductors: Mn/Co-doped ZnO nanorods as case study. J. Mater Chem. 18 (2008) 5208. https://doi.org/10.1039/B808361D

[48] Md. Nasrul, Mia Haque, Md. Firos Pervez, Md. Khalid Hossain, Rahman Mohammad Reefaz, M. Jalal, Uddin, Md. Al Mashud Abdullah, Ghosh Himangshu Kumar and Hoq Mahbubul. Influence of Mg content on tailoring optical bandgap of Mg doped ZnO thin film prepared by sol-gel method. Results in Physics. 7 (2017) 2683-2691. https://doi.org/10.1016/j.rinp.2017.07.047

[49] J. Li, D. Yang and X. Zhu. Effects of aging time and annealing temperature on structural and optical properties of sol-gel ZnO thin films. AIP Adv. 7 (2017) 065213. https://doi.org/10.1063/1.4985753

[50] K. Shimada, N. Takahashi, Y. Nakagawa, T. Hiramatsu and H. Kato. Nonlinear characteristics of structural properties and spontaneous polarization in wurtzite $Mg_xZn_{1-x}O$: A first-principales study. Phys Review B. 88 (2013) 75203. http://doi:10.1103/PhysRevB.88.075203

[51] U. Ögzür, Y.I. Alivov, C. Liu, A. Teke, M.A. Rashchikov, S. Doğan and al. A comprehensive review of ZnO materials and devices. Journal of Applied Physics. 98 (2005) 1-103. http://doi:10.1063/1.1992666

[52] S. Yang and Y. Zhang. Structural, optical and magnetic properties of Mn doped ZnO thin films prepared by sol-gel. Journal of magnetism and magnetic materials. 334 (2013) 52-58. http://doi:10.1016/j.jmmm.2013.01.026

[53] P. Veluswamy, S. Sathiyamoorthy, K.H. Chowdary, O. Muthusamy, K. Krishnamoorthy, T. Takeuchi and H. Ikeda. Morphology dependent thermal conductivity of ZnO nanostructures prepared via a green approach. Journal of Alloys and Compounds. 695 (2017) 888-894. http://dx.doi.org/10.1016/j.jallcom.2016.10.196

[54] Dhruvashi, M. Tanemura and P.K. Shishodia. Ferromagnetism in sol-gel derived ZnO:Mn nanocrystalline thin films. Advanced Materials letter. 7 (2016) 116-122. http://Doi:10.5185/amlett.2016.5966

[55] R.R. Prabhakar, N. Mathews, K.B. Jinesh, K.R.G. Karthik, S.S. Pramana, B. Varghese, C.H. Sow and S. Mhaisalkar. Efficient multispectral photodetection using Mn doped ZnO nanowires. J Mater. Chem. 22 (2012) 9678. http://dx.doi.org/10.1039/c2jm16698d

[56] R. Sankar Ganesh, E. Durgadevi, M. Navaneethan, V.L. Patil, S. Ponnusamy, C. Muthamizhchelvan, S. Kawasaki, P.S. Patil and Y. Hayakawa. Low temperature ammonia gas sensor based on Mn doped ZnO nanoparticle decorated microspheres. Journal of Alloys and Compounds. 721 (2017) 182-190. https://doi.org/10.1016/j.jallcom.2017.05.315

[57] B. Sambandam, R.J.V. Michael and P.T. Manoharan. Oxygen vacancies and intense luminescence in manganese loaded ZnO microflowers for visible light water splitting. Nanoscale. 7 (2015) 13935-13942. http://dx.doi.org/10.1039/C5NR02666K

[58] V. Kumar, H.C. Swart, S. Som, V. Kumar, A. Yousif, A. Pandey, S.K.K. Shaat and O.M. Ntwaeaborwa. The role of growth atmosphere on the structural and optical quality of defect free ZnO films for strong ultraviolet emission. Laser Phys. 24 (2014) 105704. http://Doi:10.1088/1054-660X/24/10/105704

[59] H. Ren, G. Xiang, G. Guand and X. Zhang. Enhancement of ferromagnetism of ZnO:Co nanocrystals by post-annealing treatment: The role of oxygen interstitials and zinc vacancies. Materials Latters. 122 (2014) 256. http://Doi:10.1016/j.matlet.2014.02.063

[60] Manoj Kumar, Kuldeep Negi, Suvarcha Chauhan, Ahmad Umar, Ramesh Kumar, Yoshitake Masuda, Mohinder Singh Chauhan and Rajni. Synthesis, Characterization, Photocatalytic and Sensing Properties of Mn-Doped ZnO Nanoparticles. Journal of Nanoscience and Nanotechnology. 19 (2019) 8095–8103. http://doi:10.1166/jnn.2019.16758

[61] F.M. Mwema, E.T. Akinlabi, O.P. Oladijo, O.S. Fatoba, S.A. Akinlabi and Ş. Ţălu, Advances in manufacturing analysis: fractal theory in modern manufacturing. In "Modern Manufacturing Processes", 1st edition, section 1, chapter 2, pages 13-39. Edited by: Kaushik Kumar, J. Paulo Davim. Published by Woodhead Publishing Reviews: Mechanical Engineering Series an imprint of Elsevier, USA, 2020. http://DOI:10.1016/B978-0-12-819496-6.00002-6

[62] Mohammad Reza Khanlary, Vahid Vahedi and Ali Reyhani. Synthesis and Characterization of ZnO Nanowires by Thermal Oxidation of Zn Thin Films at Various Temperatures. Molecules. 17 (2012) 5021-5029. http://doi:10.3390/molecules17055021

[63] Zhou Zhang, Jia Bao Yi, Jun Ding, Lai Mun Wong, Hwee Leng Seng, Shi Jie Wang, Jun Guang Tao, Gong Ping Li, Guo Zhong Xing, Tze Chien Sum, Cheng Hon Alfred Huan and Tom Wu. Cu-Doped ZnO Nanoneedles and Nanonails: Morphological Evolution and Physical Properties. J. Phys. Chem. C. 112 (2008) 9579–9585. https://doi.org/10.1021/jp710837h

[64] J. Li, D. Yang and X. Zh. Effects of aging time and annealing temperature on structural and optical properties of sol-gel ZnO thin films. AIP Adv. 7 (2017) 065213. https://doi.org/10.1063/1.4985753

[65] B. Hadzic, N. Romcevic, M. Romcevic, I. Kuryliszyn-Kudelska, W. Dobrowolski, U. Narkiewicz, D. Sibera. Raman study of surface optical phonons in hydrothermally obtained ZnO(Mn) nanoparticles. Optical Materials. 58 (2016) 317-322. https://doi.org/10.1016/j.optmat.2016.03.033

[66] K.A. Avramenko, V.P. Bryksa, T.L. Petrenko, V.P. Kladko, H.V. Stanchu, A.E. Belyaev, C. Deparis, J. Zuñiga-Pérez and C. Morhain. Influence of strain relaxation on the relative orientation of ZnO and ZnMnO wurtzite lattice with respect to sapphire substrates. Materials Research Express. 3 (2016) 095902. http://doi:10.1088/2053-1591/3/9/095902

[67] O. Kolomys, S. Rarata, P. Lytvyn, O. Khyzhun, C. Chey, O. Nur, and M. Willander. Raman submicron spatial mapping of individual Mn doped ZnO nanorods. Nanoscale Research Letters. 12 (2017) 75. https://doi.org/10.1186/s11671-017-2127-4

[68] H. Yadav, K. Sreenivas, R. Katiyar and V. Gupta. Defect induced activation of raman silent modes in rf cosputtered Mn doped ZnO thin films. Journal of Physics D: Applied Physics. 40 (2007) 6005. https://doi:10.1088/0022-3727/40/19/034

[69] Mahmoud Zolfaghari, Hamdallah Puladiana, Forogh Abazaria. Raman Study of Mn doped ZnO nanoparticle Proceedings of the 4th International Conference on Nanostructures (ICNS4) 12-14 March, Kish Island, Iran. (2012) 396-397.

[70] D. Toloman, A. Mesaros, A. Popa, O. Raita, T. Silipas, B. Vasile, O. Pana and L. Giurgiu. Evidence by epr of ferromagnetic phase in Mn doped ZnO nanoparticles annealed at different temperatures. Journal of Alloys and Compounds. 551 (2013) 502 – 507. https://doi.org/10.1016/j.jallcom.2012.10.183

[71] J. Wang, G. Huang, X. Zhong, L. Sun, Y. Zhou and E. Liu. Raman scattering and high temperature ferromagnetism of Mn doped ZnO nanoparticles. Applied Physics Letters. 88 (2006) 252502–252502. https://doi.org/10.1063/1.2208564

[72] R. Cuscó, E. Alarcon Llado, J. Ibáñez, L. Artús, J. Jimenez, B. Wang and M. Callahan. Temperature dependence of raman scattering in ZnO. Phys. Rev. B. 75 (2007) 165202. https://doi.org/10.1103/PhysRevB.75.165202

[73] A. Khan. Raman spectroscopic study of the ZnO nanostructures. J Pak Mater Soc. 4 (2010) 1-9.

[74] M. Boshta, M.O. Abou-Helal, D. Ghoneim, N.A. Mohsen and R.A. Zaghloul. The photocatalytic activity of sprayed $Zn_{1-x}Mg_xO$ thin films. Surface Coating Technology. 205 (2010) 271-274. https://doi.org/10.1016/j.surfcoat.2010.06.039

[75] Z.H. Ruan, Y. Yuan, X.X. Zhang, Y. Shuai and H.P. Tan. Determination of optical properties and thickness of optical thin film using stochastic particle swarm optimization Solar Energy. 127 (2016) 147-158. http://dx.doi.org/10.1016/j.solener.2016.01.027

[76] Jiawei Gong and Sumathy Krishnan. Mathematical Modeling of Dye-Sensitized Solar Cells. Dye-Sensitized Solar Cells. (2019) 51-81. https://doi.org/10.1016/B978-0-12-814541-8.00002-1

[77] Anderson Janotti and G. Chris Van de Walle. Fundamentals of zinc oxide as a semiconductor. REPORTS ON PROGRESS IN PHYSICS. 72 (2009) 126501. http://doi:10.1088/0034-4885/72/12/126501

[78] A. Goktas, F. Aslan and A. Tumbul. Nanostructured Cu-doped ZnS polycrystalline thin films produced by a wet chemical route: the influences of Cu doping and film thickness on the structural, optical and electrical properties. J Sol-Gel Sci Technol. 75 (2015) 45–53. https://doi.org/10.1007/s10971-015-3674-8